DNS of viscoelastic turbulent channel flow with rectangular orifice at low Reynolds number

Takahiro Tsukahara*, Tomohiro Kawase, Yasuo Kawaguchi

Department of Mechanical Engineering, Tokyo University of Science, 2641 Yamazaki, Noda-shi, Chiba 278-8510 Japan

Abstract

Direct numerical simulations of turbulent viscoelastic-fluid flow in a channel with a rectangular orifice were performed to investigate the influence of viscoelasticity on turbulence statistics and turbulent structures downstream of the orifice. The geometry considered is periodic rectangular orifices with 1:2 expansion. The constitutive equation follows the Giesekus model, valid for a polymer (or surfactant) solutions, which are generally capable of reducing the turbulent frictional drag in a smooth channel. The friction Reynolds number and the Weissenberg number were set to 100 and 20–30, respectively. A drag reduction of about 20% was achieved in the viscoelastic flows. The onset Reynolds number for the transition from a symmetric to an asymmetric state was found to be shifted to higher values than that for the Newtonian flow. In the viscoelastic flow, the turbulent kinetic energy was decreased and fewer turbulent eddies were observed, as the Kelvin-Helmholtz vortices were quickly damped. Away from the orifice, quasi-streamwise vortices in the viscoelastic flow were sustained for a longer period, accompanied by energy exchange from elastic energy of the viscoelastic fluid to kinetic energy.

Keywords: Direct numerical simulation, Drag reduction, Non-Newtonian fluid, Orifice, Turbulence, Viscoelasticity

*Corresponding author
Email address: tsuka@rs.noda.tus.ac.jp (Takahiro Tsukahara)

Please cite this article as: Tsukahara, T., et al. DNS of viscoelastic turbulent channel flow with rectangular orifice at low Reynolds number. Int. J. Heat Fluid Flow, Vol. 32 (2011), 529–538. doi:10.1016/j.ijheatfluidflow.2011.02.009

1. Introduction

It is common knowledge that surfactant additives or polymers can suppress turbulence and significantly reduce turbulent frictional drag, when added to a liquid flow at large Reynolds numbers. This phenomenon, the so-called Toms effect, is of practical importance and has recently been implemented in several industrial systems to save energy. In general, the solution used as a working fluid for such a drag-reducing flow is a viscoelastic liquid. However, methods to design a viscoelastic, i.e., non-Newtonian, fluid system are far from satisfactory, and there have been many studies on drag reduction by both experiment and simulation (e.g., Gyr and Bewersdorff, 1995; Procaccia et al., 2008; White and Mungal, 2008). For instance, direct numerical simulations (DNSs) of polymer-induced drag reduction were performed for isotropic turbulence (De Angelis et al., 2005), shear-driven turbulence (Vaithianathan et al., 2007), turbulent channel flow (e.g., Sureshkumar et al., 1997; Min et al., 2003; Ptasinski et al., 2003; Li et al., 2006), and boundary layers (e.g., Dimitropoulos et al., 2005; Tamano et al., 2007). The authors' group has performed DNSs on the turbulent channel flow of viscoelastic fluids using the Giesekus model for different rheological properties (Yu and Kawaguchi, 2004, 2006; Tsukahara et al., 2011). These studies considered somewhat canonical flows without any mean-flow streamline curvature. However, in practical applications of drag-reduction technology such as complicated duct flows found in district heating and cooling systems, separation and reattachment occur through, for example, sudden expansion pipe flow and ribbed or roughened channel flow. Flows of a viscoelastic fluid through an expansion geometry are also relevant in manufacturing processes such as extrusion processes and mold filling, which involve flows through channels of varying cross-section. Although the flow through expansion and/or contraction geometries has been studied in detail for the laminar regime, for both Newtonian and viscoelastic fluids (e.g., Baloch et al., 1996; Oliveira, 2003), turbulent viscoelastic flow through such geometries has received much less attention.

Recently, Newtonian fluids in a turbulent regime were investigated numerically. Makino et al. (2008) carried out DNSs of the turbulent Newtonian-fluid flow in a channel with periodic two-dimensional ribs, i.e., rectangular orifices. El Khoury et al. (2010) considered a similar problem but for a single thin-plate obstruction without periodic repeating. However, there have been few studies on the drag-reducing effect for turbulent flow in complicated flow

geometries, and in particular, to the authors' knowledge there has never been any DNS of turbulent viscoelastic flow with an orifice. Some authors (e.g., Pak et al., 1990; Poole and Escudier, 2003, 2004; Poole et al., 2005) carried out experiments on the flow through a sudden expansion, but focused on the mean flow, which could cause an asymmetric flow pattern even when the geometry itself is symmetric. It is practically required to elucidate the nature of a viscoelastic turbulent flow continuously passing over obstructions. With this background, the detailed mechanism and efficiency of turbulent drag reduction for the roughened channel flow of viscoelastic fluids should be investigated.

In the present study, we performed DNSs of viscoelastic fluids in a channel with periodically repeating rectangular orifices, in order to analyze the behavior of the flow when accompanied by separation and reattachment. Major differences between the present study and published works on smooth channels are related to the streamwise variation in the flow state and the main areas where turbulence is produced. Therefore, the instantaneous vortex structures and the relevant energy transport within the strong shear layer just downstream of the orifice will be explored, as well as the mean-flow properties such as drag-reduction rate and flow asymmetry. The Newtonian flow was also simulated for comparison. All of the simulations presented here were run at the same pumping pressure, i.e., a constant pressure drop (but the mean flow rate was dependent on the fluid properties).

2. Numerical procedure

The configuration of the computational domain is shown in Fig. 1. A periodically repeating spatial unit with a rectangular orifice was simulated employing the periodic boundary conditions in the streamwise and spanwise directions. The no-slip boundary condition was applied on all the wall surfaces. In this paper, x_1 (x), x_2 (y) and x_3 (z) denote the streamwise, the wall-normal, and the spanwise components, respectively. The direct-forcing immersed boundary method (Fadlun et al., 2000) was employed on/inside the plates on each side of the orifice. The non-dimensional governing equations are the equation of incompressible continuity:

$$\frac{\partial u_i^+}{\partial x_i^*} = 0, \tag{1}$$

the Navier-Stokes equation:

$$\frac{\partial u_i^+}{\partial t^*} + u_j^+ \frac{\partial u_i^+}{\partial x_j^*} = -\frac{\partial p^+}{\partial x_i^*} + \frac{\beta}{Re_{\tau 0}} \frac{\partial^2 u_i^+}{\partial x_j^* \partial x_j^*} + \frac{1-\beta}{We_{\tau 0}} \frac{\partial c_{ij}^+}{\partial x_j^*} - F_i^*, \tag{2}$$

and the constitutive equation based on the Giesekus model (Giesekus, 1982):

$$\frac{\partial c_{ij}^+}{\partial t} + \frac{\partial u_m^+ c_{ij}^+}{\partial x_m^*} = \frac{\partial u_i^+}{\partial x_m^*} c_{mj}^+ + \frac{\partial u_j^+}{\partial x_m^*} c_{mi}^+ - \frac{Re_{\tau 0}}{We_{\tau 0}} \cdot \left[c_{ij}^+ + \alpha (c_{im}^+ - \delta_{im})(c_{mj}^+ - \delta_{mj}) - \delta_{ij} \right], \tag{3}$$

where t, u_i, p and c_{ij} denote the time, the velocity vector $(u_1, u_2, u_3) = (u, v, w)$, the pressure, and the conformation tensor, respectively. In Eq. (2), $\beta = \eta_s/\eta_0$ is the ratio of the solvent viscosity, η_s, to the total zero-shear-rate solution viscosity, η_0, where $\eta_s - \eta_0$ is the additive contribution to the solution viscosity. The additional term of F_i in Eq. (2) represents the body force vector per unit volume for the immersed boundary method. The quantities with superscript $(^+)$ indicate that they are normalized by η_0 and/or $u_{\tau 0}$, which is derived from the mean pressure gradient through the computational volume, $-\partial \overline{p}/\partial x$, in the case of a smooth channel without any ribs, i.e.,

$$u_{\tau 0} = \sqrt{\frac{\tau_{w0}}{\rho}} = \sqrt{\frac{\delta}{\rho} \cdot \left| \frac{\partial \overline{p}}{\partial x} \right|}, \tag{4}$$

where τ_{w0} is the wall shear stress for a non-obstructed plane channel flow, ρ is the density, and δ is the channel half-width. The superscript $(^*)$ represents non-dimensionalization by δ: e.g., $y^* = y/\delta$.

The friction Reynolds number and the Weissenberg number are defined as respectively $Re_{\tau 0} = \rho u_{\tau 0} \delta/\eta_0$ and $We_{\tau 0} = \rho \lambda u_{\tau 0}^2 \delta/\eta_0$ based on the additive relaxation time λ. The simulations were carried out for $Re_{\tau 0} = 100$, and two values of $We_{\tau 0}$ were tested. As mentioned in the previous section, a constant pressure drop (between $x = 0$ and $x = 12.8\delta$) was imposed in the current DNSs, and thus the flow rate can be changed dependently on the fluid properties. In order to investigate the effects of viscoelasticity and drag-reduction rate, a Newtonian-fluid flow in the same configuration was also calculated. Note that when $We_{\tau 0} = 0$ and $\beta = 1$, Eq. (2) reduces to the common equation as for a Newtonian fluid.

For the spatial discretization, the finite difference method was used. A numerical scheme with the 4th-order central scheme was employed in the x and z directions and the 2nd-order accuracy was in the y direction. When we attempt to solve the viscoelastic flow equations numerically, a new difficulty arises that is absent in Newtonian flows: the transport equation of Eq. (3) for the conformation tensor is hyperbolic nonlinear and hence will typically produce oscillatory behavior. To minimize this problem, flux limiter terms can be introduced into the method, based on the theory of total-variation diminishing (TVD) methods, in which a suitable amount of artificial dissipation is added locally to dampen high-frequency modes. In our simulations, the MINMOD flux-limiter scheme was applied to the convective term in Eq. (3) to stabilize the present simulations. This scheme is a composite numerical scheme consisting of the second-order upwind, central differencing and first-order upwind schemes, the switch between them being controlled by a convection boundedness criterion: see Yu and Kawaguchi (2004), who reported that the MINMOD scheme stabilized the simulation of viscoelastic flow at high Weissenberg number, whereas the artificial diffusion scheme required large artificial diffusivity to stabilize the calculation.

By using the same obstruction as Makino et al. (2008), the blockage ratio of the rectangular orifice is 1:2, i.e., the distance between the channel surface and the orifice edge is 0.5δ. The computational domain volume is $12.8\delta \times 2\delta \times 6.4\delta$ in the streamwise, wall-normal, and spanwise directions, respectively. The grid size is $128 \times 128 \times 128$, giving mesh spacings of $\Delta x^+ = 10.0$, $\Delta z^+ = 5.0$, and $\Delta y^+ = 0.31$–3.01, with a nonuniform hyperbolic tangent stretching factor used in the wall-normal direction.

Time advancement was done by the 3rd-order Runge-Kutta method, but the 2nd-order Crank-Nicolson method was used for the viscous terms in the y direction. All present DNSs were run from an arbitrary initial flow field and thereafter allowed to evolve towards a statistically steady state. Statistics were gathered for $200\delta/u_{\tau 0}$ after the flow field first had evolved into a statistically steady state, sampling was taken every $2\delta/u_{\tau 0}$.

3. Results and discussion

3.1. Streamwise mean velocity

Figure 2 shows the mean (time-spanwise averaged) streamwise velocity profiles at different streamwise positions along the channel. Note again that, in the present simulations, the orifice with the thickness of 0.1δ is located at

$x = 6.4\delta$ in the streamwise direction (also shown in Fig. 1). In the region from $x^* = 5.0$–6.5, no considerable difference in the mean-velocity distribution is found between the Newtonian and viscoelastic fluids, although the magnitude of velocity in the viscoelastic flow is slightly larger than for the other. Two local peaks observed in the profile at $x^* = 6$ were attributed to the flow contraction. From $x^* = 7.0$ to 8.5, there appears a strong shear layer at the height of the orifice edge on each side (top and bottom half) of the channel. It can be seen that the strong shear layers for the viscoelastic flow are extended towards each wall compared to the Newtonian case, while the velocity in the core region (i.e., the channel center) is unchanged between these two cases. Therefore, the mean velocity gradient within the shear layer is less steep in the viscoelastic flow than the Newtonian flow. Away from the orifice ($x^* \geq 11$), the mean velocity in the core region of the viscoelastic flow is clearly larger than that of the Newtonian flow. Here, let us recall that the same constant pressure drop throughout the channel was imposed in both cases, where the near-wall velocity gradient would be unchanged (although, strictly speaking, the near-wall velocity gradient for the viscoelastic flow was slightly smaller due to existence of the viscoelastic stress). Indeed, the velocity profiles in the near-wall region become almost identical and those in the core region reveal clear differences in the two flows. This difference corresponds to increases in the bulk mean velocity u_m and the bulk Reynolds number, $Re_\mathrm{m} = 2u_\mathrm{m}\delta/\eta_0$ (Table 1), as a consequence of the fluid being viscoelastic. In other words, the turbulent frictional drag is expected to be decreased in the viscoelastic flow field.

The drag coefficient is defined as,

$$C_d = \frac{\Delta p}{L_x}\frac{\delta}{\frac{1}{2}\rho u_\mathrm{m}^2} = \frac{2}{u_\mathrm{m}^{+2}} \tag{5}$$

where Δp is the time-averaged pressure drop from $x = 0$ to L_x. The drag coefficient C_d contains the form drag by the orifice and the frictional drag of all surfaces. The values obtained by the present simulations are given in Table 1, which also shows the drag-reduction rate:

$$DR\% = \frac{C_{d\mathrm{Newt}} - C_{d\mathrm{visc}}}{C_{d\mathrm{Newt}}}, \tag{6}$$

where the suffixes 'Newt' and 'visc' stand for values referring to a Newtonian flow and a viscoelastic flow, respectively. In the present conditions, the

flows exhibit a considerable drag reduction of about 20% with respect to the Newtonian flow at the same magnitude of pressure drop. It is worth noting that the $DR\%$ obtained for $We_{\tau 0} = 30$ is 1% lower than that for $We_{\tau 0} = 20$; here, the statistical uncertainty about C_d is less than 0.2%. In general, an increase in the Weissenberg number reduces the contribution of turbulence to frictional drag for a smooth channel (without any obstruction), resulting in a higher $DR\%$ (Li et al., 2006; Yu and Kawaguchi, 2006; Tsukahara et al., 2011). As will be evident from the result that follows, the contribution of turbulence for $We_{\tau 0} = 30$ is indeed reduced throughout the channel. However, for the present flows with the bluff body, the form drag, that depends mainly on the obstacle configuration, is more dominant in C_d when compared with the frictional drag. As under laminar conditions, Oliveira (2003) numerically studied the pressure loss of viscoelastic flow in symmetric expansion geometries, and reported that the pressure losses were higher for viscoelastic flows compared to relevant Newtonian cases. Therefore, the small increase in C_d, for $We_{\tau 0} = 20 \rightarrow 30$, may be attributed to the influence of enhanced viscoelastic stress.

3.2. Streamline and turbulent kinetic energy

To illustrate vortex formations, streamlines of the mean flow are depicted in Fig. 3. In both cases of the Newtonian fluid and the viscoelastic fluid, two recirculation zones (bubbles) of finite size are clearly observed to remain in each corner of the sudden expansion behind the orifice, and they are known as 'Moffatt eddies' (Alleborn et al., 1997; Shankar, 2005, and references therein). The bubbles in viscoelastic flows are thinner in the wall-normal direction compared to those in the Newtonian flow. This is particularly noticeable at high $We_{\tau 0}$, where the reattachment point has shifted upstream, owing to a stronger divergence towards the channel walls. This suggests that the swelling behavior, the so-called 'Barus effect' as one of the most important elastic properties (see, for instance, Newman and Trementozzi, 1965; Bagley and Duffey, 1970), under turbulent conditions has been demonstrated by the present DNS. This Barus effect is well known to be related to the difference in primary normal stress due to fluid elasticity.

Figure 3 also shows the contour of the turbulent kinetic energy, k^+. For $We_{\tau 0} = 20$, the magnitude of k^+ as well as the streamline pathways upstream of the orifice seems to be unchanged in comparison to those in the Newtonian flow, while k^+ in the strong shear-layer region and the downstream corner vortex appear to have shrunk in the viscoelastic flow. The decrease

in k^+ for $We_{\tau 0} = 30$ is more prominent throughout the channel, as shown in Fig. 3c. Earlier studies on smooth channel flow revealed that the Reynolds shear stress is damped more for larger Weissenberg number (Min et al., 2003; Tsukahara et al., 2011). Similarly, the Reynolds shear stress in the present viscoelastic flow is much smaller than that of Newtonian fluid flow but decreases very slowly with increasing Weissenberg number through the range $We_{\tau 0} = 20$–30 (data not shown), because the turbulent motions might be suppressed maximally at a given $Re_{\tau 0}$. After the flow reaches its maximum frictional-drag reduction state, increasing $We_{\tau 0}$ results in a further increase in the viscoelastic stress, but an additional decrease in the Reynolds shear stress can no longer be expected. Thus, the value of C_d at $We_{\tau 0} = 30$ is slightly increased. For higher Reynolds numbers, a further increase in $We_{\tau 0}$ is expected to lead to more effective drag reduction, because the contribution of the turbulent frictional drag to the total one is more dominant in high Reynolds-number turbulence.

It can be seen from Fig. 3a that the mean flow behind the orifice for the Newtonian fluid is asymmetric along the centerline of the channel. Such a phenomenon, occurring in planar expansions, can be explained by a 'Coanda effect', in which any perturbation of the flow field, pushing the main flow to one or other side of the channel, induces larger velocities and lower pressures there, and hence the asymmetry will tend to be accentuated (see, e.g., Shapira et al., 1990; Oliveira, 2003; El Khoury et al., 2010). We can observe in Fig. 3a that the flow bends towards the upper wall behind the orifice, but note that the direction of bending is determined randomly with equal probability for either direction. This mean flow pattern in the turbulent background is supposed to be a counterpart of steady asymmetric solutions in a laminar case. Several reports in the literature revealed that a laminar flow remains symmetric up to a certain Reynolds number depending on the expansion ratio, while asymmetries appear as a steady state at higher Reynolds numbers (Drikakis, 1997; Mizushima and Shiotani, 2000). According to the DNS study by Makino et al. (2008), for $Re_{\tau 0} > 20$ under the present configuration (of a symmetric channel with a 1:2 sudden expansion), the Newtonian flow should give rise to an asymmetric pattern, with a larger and a smaller recirculation zone behind the orifice. However, the mean flow for a viscoelastic fluid seems to be rather symmetric about the channel center even at $Re_{\tau 0} = 100$ as shown in Figs. 3b and 3c. Each figure reveals that the flow field has two bubbles with equal lengths behind the orifice. The mean streamlines (and also the other statistical data) were obtained by long-time

averaging after a statistically steady state was achieved in each case. So, the rather symmetric pattern in the viscoelastic flows as well as the asymmetric one in the Newtonian flow are expected to be stable solutions or to sustain for at least $\Delta T^* = 200$. It is conjectured here that the Coanda effect on the viscoelastic flow occurs at higher Reynolds numbers than that for the Newtonian case.

An asymmetric parameter of the mean flow is defined by

$$R(x) = \frac{\langle u_d(x,y) \cdot u_d(x, 2\delta - y) \rangle}{\sqrt{\langle u_d(x,y)^2 \rangle} \sqrt{\langle u_d(x, 2\delta - y)^2 \rangle}}, \tag{7}$$

$$u_d(x,y) = \overline{u}(x,y) - u_{\mathrm{m}}, \tag{8}$$

where $\overline{u}$ is the mean streamwise velocity (averaged in time and spanwise direction) and the parentheses $\langle\ \rangle$ represent averaging in the y direction from 0 to δ. When $R(x) = 1$, the velocity field is symmetric with respect to the channel center; when $R(x) = 0$, the velocity is asymmetric. Figure 4 shows the distribution of $R(x)$ along the x direction. As can be seen from this figure, the asymmetry is accentuated most strongly near the reattachment point (around $x^* = 10$). In the Newtonian flow, the asymmetry is clearly visible, but less so in a viscoelastic fluid. The flow becomes more symmetric as the Weissenberg number increases ($We_{\tau 0} = 30$), and so we conclude that the viscoelasticity negates the Coanda effect even under the turbulent flow regime. A similar finding was reported in previous studies under different conditions in the laminar flow regime (Oliveira, 2003, and reference therein).

The statistical results concerning the viscoelastic flow simulations are given in the following subsections which deal with the flow field only for $We_{\tau 0} = 20$, since this paper focuses mainly on a comparative discussion between Newtonian and viscoelastic fluids. The conclusions drawn from this comparison are consistent, at least qualitatively, with $We_{\tau 0} = 30$.

3.3. Instantaneous vortex structures behind the orifice

Figure 5 shows vortex structures in the flow fields, where a vortex is identified by the iso-surface of the second invariant, Q, of the velocity-gradient tensor, defined as

$$Q^+ = -\frac{\partial u_i'^+}{\partial x_j^+} \frac{\partial u_j'^+}{\partial x_i^+}. \tag{9}$$

In the viscoelastic-fluid flow, the number of vortices significantly decreases. Focusing on the strong shear-layer region just downstream of the orifice, the

spanwise primary Kelvin-Helmholtz (K-H) vortices are visible in Fig. 5a, but almost absent in Fig. 5b so that small-scale eddies do not appear as such. As reported by Makino et al. (2008), at this Reynolds number with the Newtonian fluid, the K-H vortices are distorted and break up into complex three-dimensional vortex structures with a lattice pattern. In the viscoelastic flow, the K-H spanwise vortices seem to decay quickly at δ downstream from the orifice, so that eddy motions, which give rise to the momentum transport, are sparse in the region from $x^* = 7.5$ to 10. This result agrees with the discussion on turbulent kinetic energy in Fig. 3. At positions away from the orifice, elongated quasi-streamwise vortices are clearly found to be maintained (at least up to $x^* = 12$) in the viscoelastic flow. In the Newtonian flow the large-scale vortices generated at each orifice edge should progressively break into small-scale eddies further downstream, whereas the quasi-streamwise vortices in the viscoelastic case are sustained for a longer period.

3.4. Anisotropy characteristic

Lumley and Newman (1977) proposed the anisotropy invariant map (AIM) to objectively quantify the level of anisotropy of turbulence, by introducing the anisotropy tensor,

$$b_{ij} = \frac{\overline{u_i' u_j'}}{2k} - \frac{1}{3}\delta_{ij}. \tag{10}$$

A plot of its second and third invariants

$$II = -\frac{b_{ij}b_{ji}}{2}, \quad III = \frac{b_{ij}b_{jk}b_{ki}}{3} \tag{11}$$

is called the AIM, where three curves bound all physically realizable turbulence, and (III, II) should always be inside the Lumley triangle, as shown in Fig. 6. In this figure, the upper straight line shows two-component (2C) turbulence and the right and left curves show axisymmetric turbulence: the right-hand curve corresponds to turbulence strained by axisymmetric expansion like a diffuser, and the left-hand curve by axisymmetric contraction like a nozzle. The intersections at $(III, II) = (0, 0)$, $(-1/108, 1/12)$, and $(2/27, 1/3)$ show isotropic turbulence, isotropic 2C turbulence, and one-component (1C) turbulence states, respectively.

According to published studies (Jovanović et al., 2006; Frohnapfel et al., 2007) using DNS and experimental data for various drag-reduced turbulent flows, the drag-reduced flow tends to increase anisotropy in the near-wall

region. Figures 7 and 8 show the AIM at the streamwise positions of $x^* = 7.0$ and 8.0, where the K-H vortex decayed in the viscoelastic fluid. Regarding the turbulence intensities, we plot them in Figs. 9 and 10 for the Newtonian and viscoelastic flows, respectively. From these results, three different types of behavior can be identified: (i) within the viscous sublayer, the bubble (recirculation zone) favors two-component isotropy, reducing the wall-normal turbulence intensity (v'_{rms}) and increasing the two components (u'_{rms} and w'_{rms}). This 2C isotropic limit state just downstream of the orifice is in good consistency with the experimental result of Fischer and co-workers reported by Jovanović and Pashtrapanska (2004) for disturbances induced by a two-dimensional roughness element attached to the wall in a laminar boundary layer. Such trajectory in the AIM that approaches the line signifying a nozzle-like flow state is a typical one of tripped near-wall turbulence and thus can not directly be compared with drag-reduced turbulence in a smooth channel. (ii) In the center of the channel all turbulence intensities tend to be comparable, resulting in a three-component (3C) isotropic turbulence, since the rate of deformation is zero. (iii) In the most important intermediate (strong shear layer) region, which includes the peak turbulence and the main turbulence producing zones, there clearly occurs an increase in anisotropy towards a one-component turbulence state, i.e., $u'_{\mathrm{rms}} > w'_{\mathrm{rms}} \approx v'_{\mathrm{rms}}$.

At $x^* = 7.0$ (where K-H vortices are generated), the typical behaviors described above can be clearly distinguished from trajectories in the AIM regardless of the fluid (Figs. 7a and 8a). On the other hand, at $x^* = 8.0$ the 1C anisotropy is relaxed in the case of the Newtonian flow, but still remains in the viscoelastic case (Figs. 7b and 8b). In the latter case, the anisotropy at $x^* = 8.0$ is almost the same as that at $x^* = 7.0$; moreover, at the higher Weissenberg number of 30, the anisotropy at $x^* = 8.0$ is stronger than that at $x^* = 7.0$ (figure not shown). Such a flow state, approaching the 1C limit, is similar to the near-wall state of drag-reduced turbulent flow, in which the turbulent dissipation is significantly reduced in the near-wall region. Even if we focus on downstream of the reattachment point, the trajectory for the viscoelastic flow at $x^* = 11$ is apparently closer to the 1C limit than at the same steamwise position for the Newtonian flow, as shown in Fig. 11. To compare with a smooth channel flow, also shown in the figure is the DNS result (Tsukahara et al., 2011) of turbulence with/without drag reduction, although their simulations were done at different $Re_{\tau 0}$. In the viscoelastic flow in a smooth channel, the points that correspond to the positions at the wall and the most-highly disturbed region move upwards in the direction of

the 1C limit. Also in the core region, the trajectory remains far from the 3C isotropic limit, compared to the Newtonian case. In the present viscoelastic case with the orifice, similar trends can be observed, although the point in the immediate wall vicinity remains on the 2C isotropic limit. It is interesting to note that the wall-normal height, at which the trajectory approaches the 1C limit, is found to be around the orifice edge, i.e., $y^* = 0.5$, where the turbulent kinetic energy is most enhanced due to the strong shear layer downstream of the orifice: cf. Fig. 3. This seems not to agree with the consideration in respect to the smooth channel (Frohnapfel et al., 2007) that the approach to the 1C limit occurs in the wall vicinity and leads to drag reduction. However, it is reasonable that, if the relaxation time of viscoelastic fluid is appropriately comparable to the local turbulent time scale, the turbulence would undergo considerable modification there by the viscoelasticity and reach locally a state of 1C anisotropy. For the viscoelastic flow, this suggests that the loss (or redistribution to other components) of energy in the u' component is decreased in the region of high turbulent intensity, and that the turbulent frictional drag on the surface downstream of the reattachment point should be reduced as a consequence of anisotropy in the near-wall region.

3.5. Budget of Reynolds stress

Figures 12 to 14 show the wall-normal variations of the budget terms for Reynolds stresses of $\overline{u'u'}$, $\overline{v'v'}$ and $\overline{w'w'}$ at $x^* = 7.5$, where K-H vortices break into small-scale eddies or decayed quickly. The transport equation of the Reynolds stress, $\overline{u_i'u_j'}$, is expressed as

$$\frac{\partial \overline{u_i'^+ u_j'^+}}{\partial t^+} = P_{ij} - \varepsilon_{ij} + \Pi^*_{ij} + T_{ij} + V_{ij} + E_{ij} + A_{ij}, \tag{12}$$

where

$$P_{ij} = -\overline{u_j'^+ u_k'^+}\frac{\partial \overline{u}_i^+}{\partial x_k^+} - \overline{u_i'^+ u_k'^+}\frac{\partial \overline{u}_j^+}{\partial x_k^+}, \tag{13}$$

$$\varepsilon_{ij} = 2\beta\overline{\frac{\partial u_i'^+}{\partial x_k^+}\frac{\partial u_j'^+}{\partial x_k^+}}, \tag{14}$$

$$\Pi^*_{ij} = -\overline{\left(u_i'^+\frac{\partial p^+}{\partial x_j^+} + u_j'^+\frac{\partial p^+}{\partial x_i^+}\right)}, \tag{15}$$

$$T_{ij} = -\frac{\partial}{\partial x_k^+}\overline{u_i'^+ u_j'^+ u_k'^+}, \tag{16}$$

$$D_{ij} = \beta \frac{\partial^2}{\partial x_k^+ \partial x_k^+} \overline{u_i'^+ u_j'^+}, \tag{17}$$

$$E_{ij} = \frac{1-\beta}{We_{\tau 0}} \overline{\left(u_i'^+ \frac{\partial c_{jk}'^+}{\partial x_k^+} + u_j'^+ \frac{\partial c_{ik}'^+}{\partial x_k^+} \right)}, \tag{18}$$

$$A_{ij} = -\overline{u}_k^+ \frac{\partial \overline{u_i'^+ u_j'^+}}{\partial x_k^+}. \tag{19}$$

Here, the terms in the right-hand side of Eq. (12) are (in order from left to right) the production, the dissipation, the velocity pressure-gradient correlation, the turbulent transport, the viscous diffusion, the viscoelastic contribution, and the advection terms. The term of Π_{ij}^* can be split into the pressure strain term ϕ_{ij} and the pressure diffusion term Π_{ij}:

$$\phi_{ij} = \overline{p'^+ \left(\frac{\partial u_i'^+}{\partial x_j^+} + \frac{\partial u_j'^+}{\partial x_i^+} \right)}. \tag{20}$$

$$\Pi_{ij} = \frac{\partial \overline{p'^+ u_i'^+}}{\partial x_j^+} + \frac{\partial \overline{p'^+ u_j'^+}}{\partial x_i^+}. \tag{21}$$

It is well-known that the former plays a dominant role in the redistribution of energy.

The budget terms for $\overline{u'u'}$ are shown in Fig. 12 for both the Newtonian and the viscoelastic flows. Note that their vertical scales, also in Figs. 13 and 14, are different. The production, the turbulent transport, the pressure strain, and the advection terms are dominant, especially, in the region from $y^* = 0.5$ to 0.8, because the velocity gradient in this region becomes large due to the velocity difference between the main flow and the recirculation zones, as shown in Fig. 3. As can be seen from Eq. (13), such a large velocity gradient gives rise to a large value of P_{11}. In the viscoelastic flow, the peak in P_{11} is smaller than that in the Newtonian flow and locally decreases at $y^* = 0.55$. At the same height, the turbulent transport, T_{11}, is also damped and is slightly positive, so the kinetic energy is transferred from other heights of local peaks in P_{11}. These phenomena occur due to the viscoelastic contribution of the fluid. The DNS study on a smooth channel flow by Min et al. (2003) revealed that the turbulent kinetic energy near the wall, i.e., at the high-P_{11} height, was absorbed by the polymer and transformed into elastic energy, when drag reduction occurs. Then, this elastic energy near the wall

was released as turbulent kinetic energy or was dissipated in the buffer and log layers. Thus, the polymer actively intervenes in the energy transfer. A similar process can be found in the strong shear layer with the viscoelastic fluid. The viscoelastic contribution, E_{11}, is negative at $y^* = 0.6$ and becomes positive at $y^* = 0.45$ and 0.7. The distributions of the turbulent and molecular diffusions (T_{11} and D_{11}) show opposite manners, revealing that these terms always serve to transport energy from the peak production zone to other areas. It is interesting to note that the distribution of E_{11} is similar to those of T_{11} and D_{11} in the Newtonian flow.

The budgets for $\overline{v'v'}$ and $\overline{w'w'}$ are shown in Figs. 13 and 14, respectively. Note again that the vertical scale for the viscoelastic flow [in (a)] is half of that for the Newtonian flow [in (b)]. For both components, the dominant terms are the pressure strain, the dissipation, and the advection terms. As for $\overline{v'v'}$, the pressure strain term of ϕ_{22} has a peak at $y^* = 0.63$ (Fig. 13a), while in Fig. 13b it has two peaks at $y^* = 0.46$ and 0.65. The positions of these peaks are in agreement with the peaks of the production for $\overline{u'u'}$ in each flow. On the other hand, there exists a single peak in ϕ_{33} for both flows, although the positions are different between them.

As shown in Figs. 13b and 14b, the viscoelastic contribution terms of E_{22} and E_{33} are found to cause a loss of turbulent kinetic energy, which is changed into elastic energy and released downstream. Consequently, the decreases in A_{22} and A_{33} are more significant than those in the pressure strain terms. In other words, a large amount of energy, which should be convected by the advection term in the case of the Newtonian flow, is transferred downstream by the viscoelastic contribution through energy exchanges. This process is consistent with other evidence that quasi-streamwise vortices can persist downstream (see Fig. 5b), since the elastic energy stored near the orifice is released into turbulent kinetic energy away from the orifice. This means that the decrease in the production of turbulent kinetic energy is compensated by the increase in energy transfer from polymer elastic energy to turbulent kinetic energy, in accordance with existing DNS studies on a smooth channel flow (Min et al., 2003; Tsukahara et al., 2011).

As mentioned above, the K-H vortex in the viscoelastic flow decays immediately at $x^* = 7.5$ and this suppression results in low turbulent kinetic energy there and downstream (see Figs. 3 and 5). The production of turbulent kinetic energy, P_k, is also expected to be significantly decreased there. Figure 16 shows the streamwise distribution of P_k, downstream of the orifice, at the height of $y^* = 0.5$ (the same as the orifice edge). The magnitude of

P_k in the viscoelastic flow remarkably decreases in the region from $x^* = 7.5$ to 10.5, while it becomes slightly larger than that for the Newtonian flow in the other regions. Assuming that $\overline{w} = 0$ and $\partial/\partial z = 0$, the expression for P_k is written as,

$$\begin{aligned} P_k &= -\overline{u'^+u'^+}\frac{\partial \overline{u^+}}{\partial x^+} - \overline{v'^+u'^+}\frac{\partial \overline{v^+}}{\partial x^+} \\ &\quad -\overline{u'^+v'^+}\frac{\partial \overline{u^+}}{\partial y^+} - \overline{v'^+v'^+}\frac{\partial \overline{v^+}}{\partial y^+}. \end{aligned} \tag{22}$$

As expected, the velocity gradient of $\partial\overline{u}/\partial y$ is much larger than the other velocity gradients (see Fig. 15). Thus, the third term in Eq. (22) is the dominant term in the production. Figure 16 also shows the distribution of the Reynolds shear stress $-\overline{u'v'}$, which appears in the third term of Eq. (22). It can be seen that $-\overline{u'v'}$ in the viscoelastic flow is clearly damped, as is the production term, and shifted downstream. It is for this reason that the production of turbulent kinetic energy is suppressed in the viscoelastic flow.

4. Conclusions

In the present study, turbulent flows of a viscoelastic fluid in a channel flow with periodic rectangular orifices were analyzed using DNS at the friction Reynolds number $Re_{\tau 0} = 100$ for the Weissenberg numbers $We_{\tau 0} = 20$ and 30, in order to investigate the effects of viscoelasticity on vortex structures, streamlines, and turbulence statistics including the drag-reduction rate.

We obtained a significant drag reduction of 18.7–19.7% in the viscoelastic flows with respect to the Newtonian flow at the same magnitude of pressure drop. The lower (or almost the same) drag reduction rate was achieved in the case of $We_{\tau 0} = 30$, although the turbulent kinetic energy was more decreased throughout the channel than that for $We_{\tau 0} = 20$. The onset Reynolds number for the transition from a symmetric to an asymmetric state is shifted to higher values (but still unknown). Although the Coanda effect should occur for $Re_{\tau 0} > 20$ according to Makino et al. (2008), the present viscoelastic flows were rather symmetric about the channel center even at $Re_{\tau 0} = 100$. The viscoelasticity is therefore a stabilizing factor in suppressing the Coanda effect.

The vortex region of the mean-flow streamline behind the orifice was observed to be smaller in the viscoelastic flow, compared to the Newtonian case.

Thus the Barus effect under turbulent conditions was successfully demonstrated. The turbulent kinetic energy and the number of vortices decreased in the viscoelastic case, because the spanwise Kelvin-Helmholtz vortices triggered by the orifice edge were quickly damped. Moreover, a large amount of turbulent kinetic energy, which should be convected by the mean-flow advection in the case of the Newtonian flow, was transferred into elastic energy of the viscoelastic fluid and was released downstream through energy-exchange processes. Away from the orifice, quasi-streamwise vortices in the viscoelastic case were sustained and propagated for a longer period. The decrease in the production of turbulence in the viscoelastic flow was attributed to the decrease in the generation of spanwise Kelvin-Helmholtz vortices, which contributed to the Reynolds shear stress. The redistribution to other components of energy in the streamwise velocity fluctuation for the viscoelastic flow was decreased in the region of high turbulent intensity, i.e., the strong shear layer just downstream of the orifice, and thus lead to an increase in the anisotropy of the Reynolds stress.

Although the present Reynolds number was considerably lower than that corresponding to conditions under which drag reduction in practical flow systems is observed with dilute additive solutions, we have demonstrated using DNS that a reduction in the drag (total pressure loss) can be achieved even in a complicated flow geometry. The above conclusions have been drawn from limited cases, however similar experimental studies will be conducted in the near future. It will also be necessary to calculate viscoelastic flows at higher Reynolds numbers with a wide range of Weissenberg numbers.

Acknowledgments

The present computations were performed with the uses of supercomputing resources at Cyberscience Center of Tohoku University and the the Earth Simulator at Japan Agency for Marine-Earth Science and Technology.

References

Alleborn, N., Nandakumar, K., Raszillier, H., Durst, F., 1997. Further contributions on the two-dimensional flow in a sudden expansion. J. Fluid Mech. 330, 169–188.

Bagley, E. B., Duffey, H. J., 1970. Recoverable shear strain and the barus effect in polymer extrusion. J. Rheol. 14, 545–553.

Baloch, A., Townsend, P., Webster, M. F., 1996. On vortex development in viscoelastic expansion and contraction flows. J. Non-Newtonian Fluid Mech. 65, 133–149.

De Angelis, E., Casciola, C. M., Benzi, R., Piva, R., 2005. Homogeneous isotropic turbulence in dilute polymers. J. Fluid Mech. 531, 1–10.

Dimitropoulos, C. D., Dubief, Y., Shaqfeh, E. S. G., Moin, P., Lele, S. K., 2005. Direct numerical simulation of polymer-induced drag reduction in turbulent boundary layer flow. Phys. Fluids 17, 011705.

Drikakis, D., 1997. Bifurcation phenomena in incompressible sudden expansion flows. Phys. Fluids 9, 76–87.

El Khoury, G. K., Pettersen, B., Andersson, H. I., Barri, M., 2010. Asymmetries in an obstructed turbulent channel flow. Phys. Fluids 22, 095103.

Fadlun, E. A., Verzicco, R., Orlandi, P., Mohd-Yusof, J., 2000. Combined immersed-boundary finite-difference methods for three-dimensional complex flow simulations. J. Comput. Phys. 161, 35–60.

Frohnapfel, B., Lammers, P., Jovanović, J., Durst, F., 2007. Interpretation of the mechanism associated with turbulent drag reduction in terms of anisotropy invariants. J. Fluid Mech. 577, 457–466.

Giesekus, H., 1982. A simple constitutive equation for polymer fluids based on the concept of deformation-dependent tensorial mobility. J. Non-Newtonian Fluid Mech. 11, 69–109.

Gyr, A., Bewersdorff, H.-W., 1995. Drag reduction of turbulent flows by additives. Kluwer Academic Pub.

Jovanović, J., Pashtrapanska, M., 2004. On the criterion for the determination transition onset and breakdown to turbulence in wall-bounded flows. Trans. ASME I: J. Fluids Eng. 126, 626–633.

Jovanović, J., Pashtrapanska, M., Frohnapfel, B., Durst, F., Koskinen, J., Koskinen, K., 2006. On the mechanism responsible for turbulent drag reduction by dilute addition of high polymers: theory, experiments, simulations, and predictions. Trans. ASME I: J. Fluids Eng. 126, 118–130.

Li, C.-F., Sureshkumar, R., Khomami, B., 2006. Influence of rheological parameters on polymer induced turbulent drag reduction. J. Non-Newtonian Fluid Mech. 140, 23–40.

Lumley, J. L., Newman, G. R., 1977. The return to isotropy of homogeneous turbulence. J. Fluid Mech. 82, 161–178.

Makino, S., Iwamoto, K., Kawamura, H., 2008. Turbulent structures and statistics in turbulent channel flow with two-dimensional slits. Int. J. Heat and Fluid Flow 29, 602–611.

Min, T., Yoo, J. Y., Choi, H., Joseph, D. D., 2003. Drag reduction by polymer additives in a turbulent channel flow. J. Fluid Mech. 486, 213–238.

Mizushima, J., Shiotani, Y., 2000. Structural instability of the bifurcation diagram for two-dimensional flow in a channel with a sudden expansion. J. Fluid Mech. 420, 131–145.

Newman, S., Trementozzi, Q. A., 1965. Barus effect in filled polymer melts. J. Appl. Polymer Sci. 9, 3071–3089.

Oliveira, P. J., 2003. Asymmetric flows of viscoelastic fluids in symmetric planar expansion geometries. J. Non-Newtonian Fluid Mech. 114, 33–63.

Pak, B., Cho, Y. I., Choi, S. U. S., 1990. Separation and reattachment of non-newtonian fluid flows in a sudden expansion pipe. J. Non-Newtonian Fluid Mech. 37, 175–199.

Poole, R. J., Escudier, M. P., 2003. Turbulent flow of a viscoelastic shear-thinning liquid through a plane sudden expansion of modest aspect ratio. J. Non-Newtonian Fluid Mech. 112, 1–26.

Poole, R. J., Escudier, M. P., 2004. Turbulent flow of viscoelastic liquids through an asymmetric sudden expansion. J. Non-Newtonian Fluid Mech. 117, 25–46.

Poole, R. J., Escudier, M. P., Oliveira, P. J., 2005. Laminar flow of a viscoelastic shear-thinning liquid through a plane sudden expansion preceded by a gradual contraction. Proc. R. Soc. A 461, 3827–3845.

Procaccia, I., L'vov, V. S., Benzi, R., Jan 2008. Colloquium: Theory of drag reduction by polymers in wall-bounded turbulence. Rev. Mod. Phys. 80 (1), 225–247.

Ptasinski, P. K., Boersma, B. J., Nieuwstadt, F. T. M., Hulsen, M. A., Van den Brule, B. H. A. A., Hunt, J. C. R., 2003. Turbulent channel flow near maximum drag reduction: simulations, experiments and mechanisms. J. Fluid Mech. 490, 251–291.

Shankar, P. N., 2005. Moffatt eddies in the cone. J. Fluid Mech. 539, 113–135.

Shapira, M., Degani, D., Weihs, D., 1990. Stability and existence of multiple solutions for viscous flow in suddenly enlarged channels. Comput. Fluids 18, 239–258.

Sureshkumar, R., Beris, A. N., Handler, R. A., 1997. Direct numerical simulation of the turbulent channel flow of a polymer solution. Phys. Fluids 9, 743–755.

Tamano, S., Itoh, M., Hoshizaki, K., Yokota, K., 2007. Direct numerical simulation of the drag-reducing turbulent boundary layer of viscoelastic fluid. Phys. Fluids 19, 075106.

Tsukahara, T., Ishigami, T., Yu, B., Kawaguchi, Y., 2011. DNS study on viscoelastic effect in drag-reduced turbulent channel flow. J. Turbulence 12, 1–25.

Vaithianathan, T., Robert, A., Brasseur, J. G., Collins, L. R., 2007. Polymer mixing in shear-driven turbulence. J. Fluid Mech. 585, 487–497.

White, C. M., Mungal, M. G., 2008. Mechanics and prediction of turbulent drag reduction with polymer additives. Ann. Rev. Fluid Mech. 40, 235–256.

Yu, B., Kawaguchi, Y., 2004. Direct numerical simulation of viscoelastic drag-reducing flow: a faithful finite difference method. J. Non-Newtonian Fluid Mech. 116, 431–466.

Yu, B., Kawaguchi, Y., 2006. Parametric study of surfactant-induced drag reduction by DNS. Int. J. Heat and Fluid Flow 27, 887–894.

Table 1: Mean-flow statistics obtained for different simulations of Newtonian and viscoelastic fluid flows.

Fluid	$We_{\tau 0}$	β	Re_{m}	C_d	$DR\%$
Newtonian	—	1.0	579	0.0597	—
Viscoelastic	20	0.8	646	0.0479	19.7
Viscoelastic	30	0.8	642	0.0485	18.7

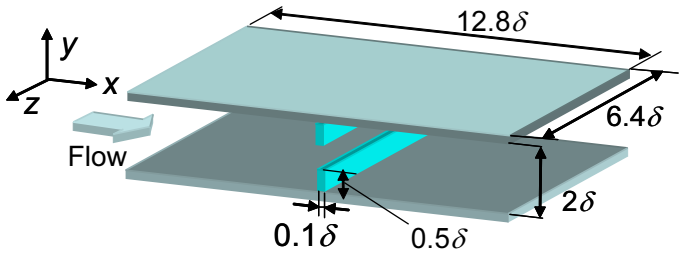

Figure 1: Configuration of the computational domain. A rectangular orifice is installed half way along the streamwise domain length.

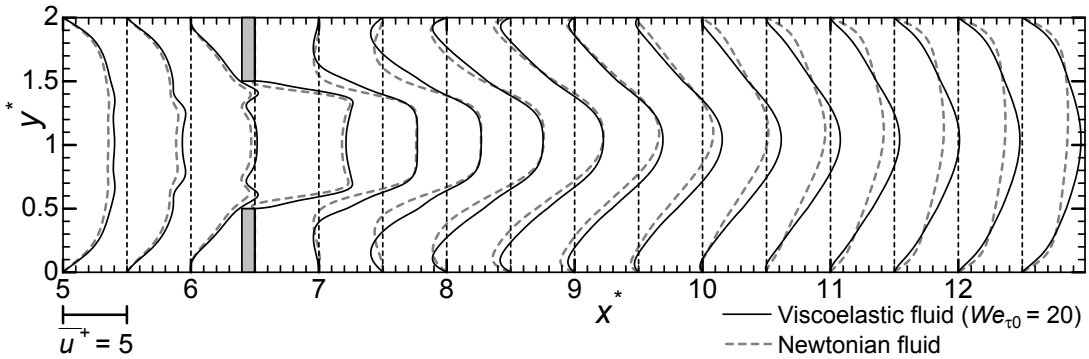

Figure 2: Mean streamwise velocity profiles at different streamwise positions.

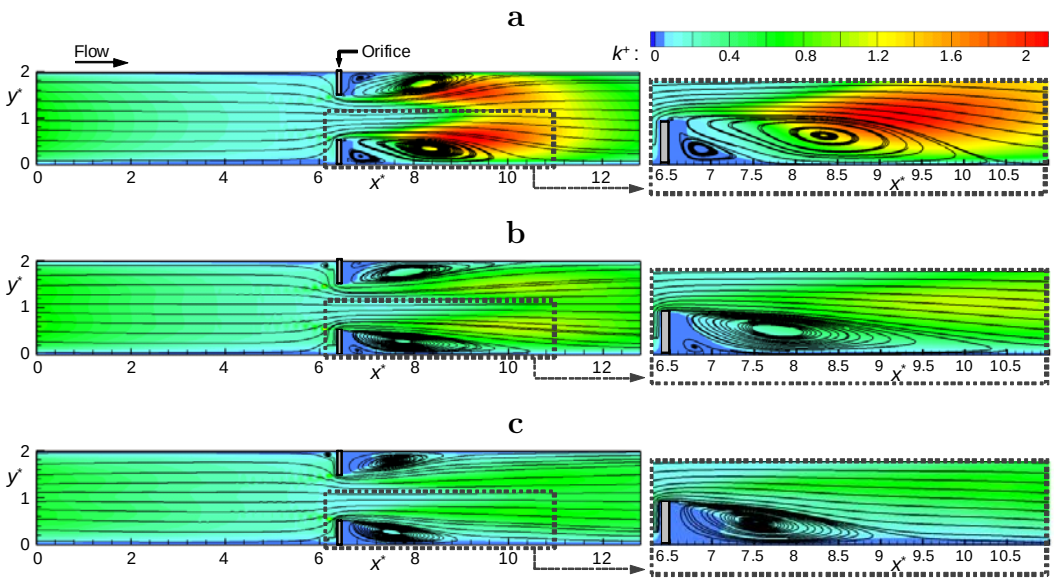

Figure 3: Averaged streamlines and contours of turbulent kinetic energy in the x-y plane. (a) Newtonian-fluid flow, (b) viscoelastic-fluid flow for $We_{\tau 0} = 20$, (c) $We_{\tau 0} = 30$.

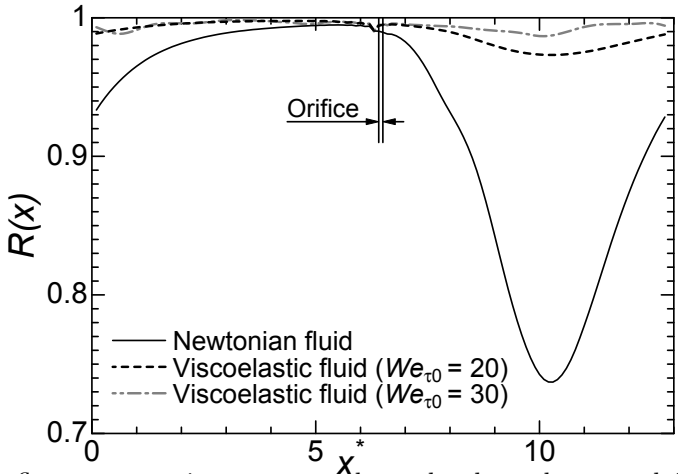

Figure 4: Mean-flow asymmetric parameter about the channel center, defined by Eq. (7), as a function of streamwise distance. The rectangular orifice is installed at $x^* = 6.4$–6.5.

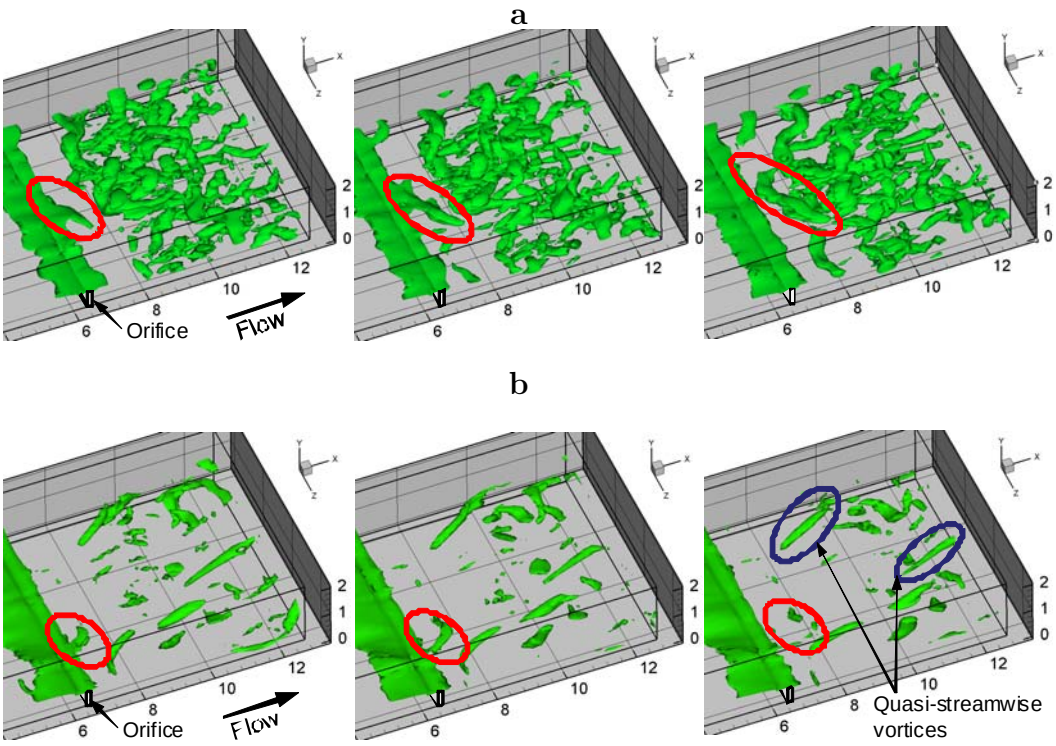

Figure 5: Temporal evolution of the flow field behind the orifice: iso-surfaces of the second invariant of the velocity gradient tensor, $Q^+ = -0.015$. For easier visualization, only the lower half of the domain is displayed. Mean flow direction is from bottom-left to top-right. Each red circle represents a Kelvin-Helmholtz vortex. (a) Newtonian-fluid flow, (b) Viscoelastic-fluid flow ($We_{\tau 0} = 20$).

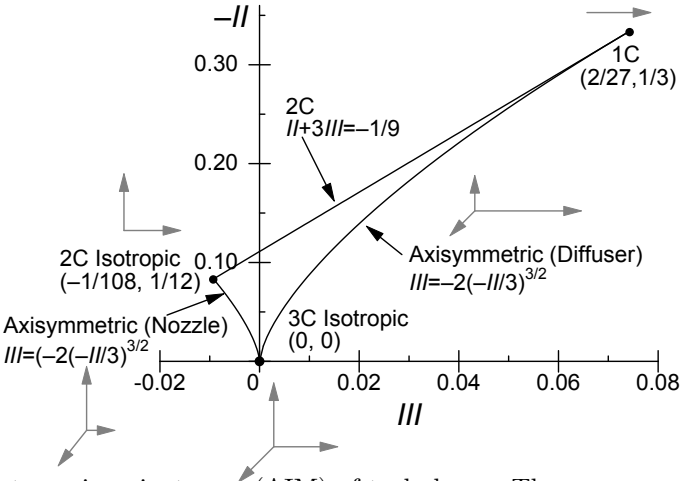

Figure 6: Anisotropy-invariant map (AIM) of turbulence. The gray arrows represent the velocity fluctuations under each of the labeled condition.

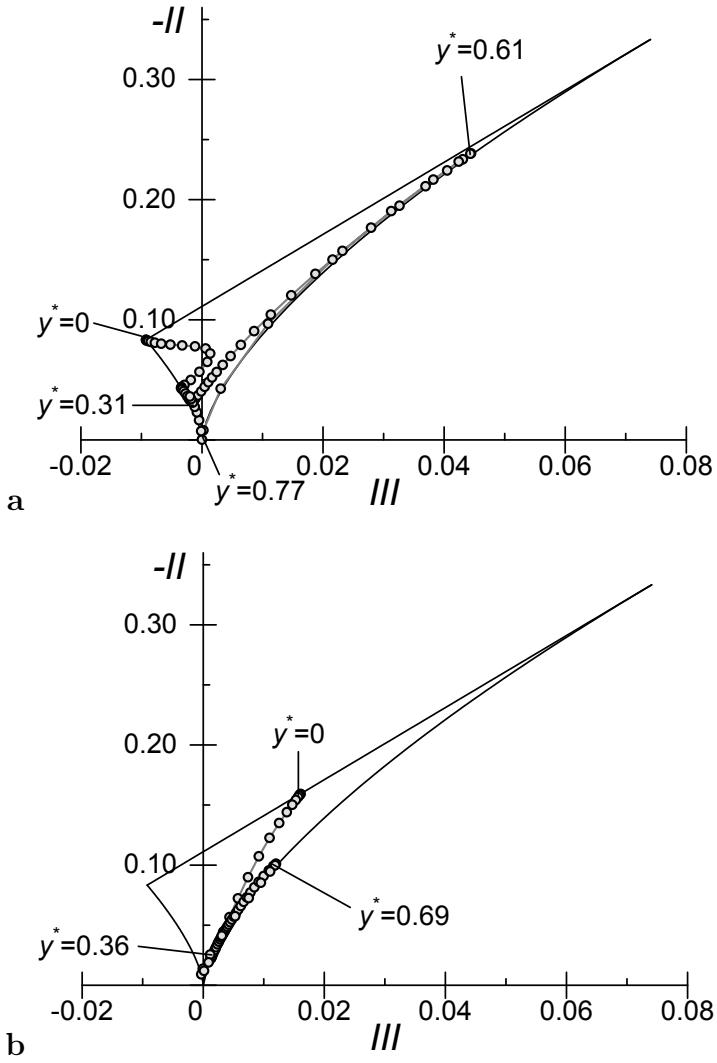

Figure 7: Reynolds-stress anisotropy invariant map for Newtonian fluid. (a) $x^* = 7.0$, (b) $x^* = 8.0$.

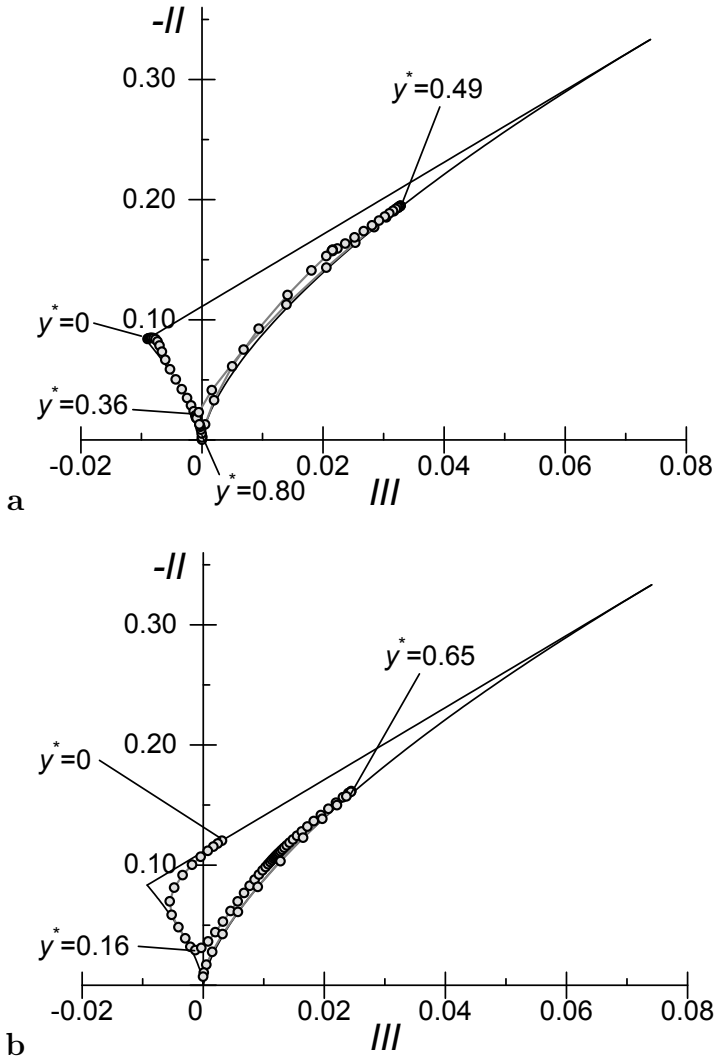

Figure 8: Same as Fig. 7, but for viscoelastic fluid at $We_{\tau 0} = 20$. (a) $x^* = 7.0$, (b) $x^* = 8.0$.

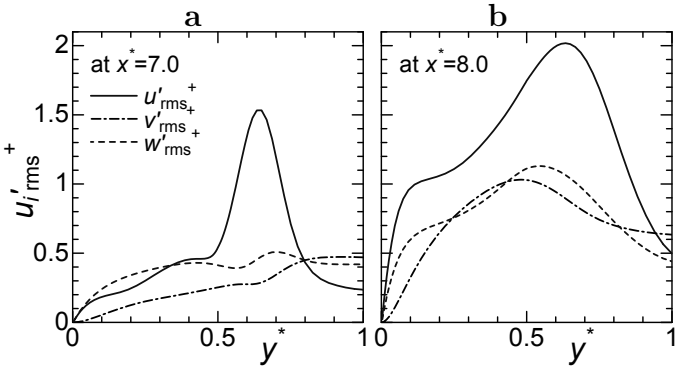

Figure 9: Wall-normal distribution of turbulence intensity at different streamwise positions for Newtonian-fluid flow.

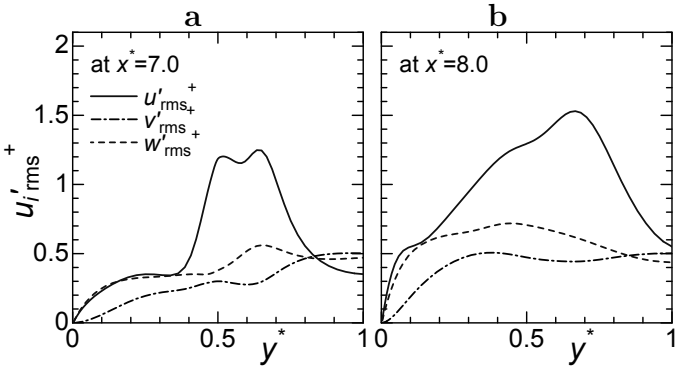

Figure 10: Same as Fig. 9, but for viscoelastic-fluid flow at $We_{\tau 0} = 20$.

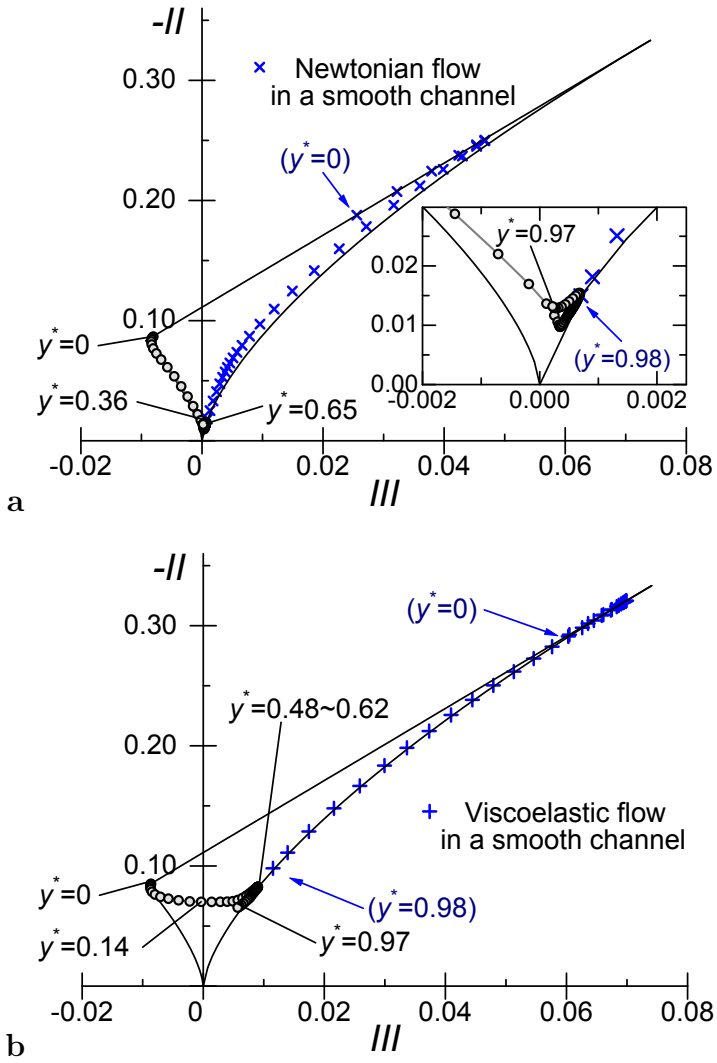

Figure 11: Reynolds-stress anisotropy invariant map at $x^+ = 11$ for (a) Newtonian fluid and (b) viscoelastic fluid at $We_{\tau 0} = 20$. For comparison, AIM for a smooth channel flow, obtained by Tsukahara et al. (2011), are also shown by the symbols $\times$ and $+$, representing the results of a Newtonian flow at $Re_{\tau 0} = 150$ and of a viscoelastic flow for $We_{\tau 0} = 30$ and $\beta = 0.5$ (yielding a drag reduction of 52%), respectively.

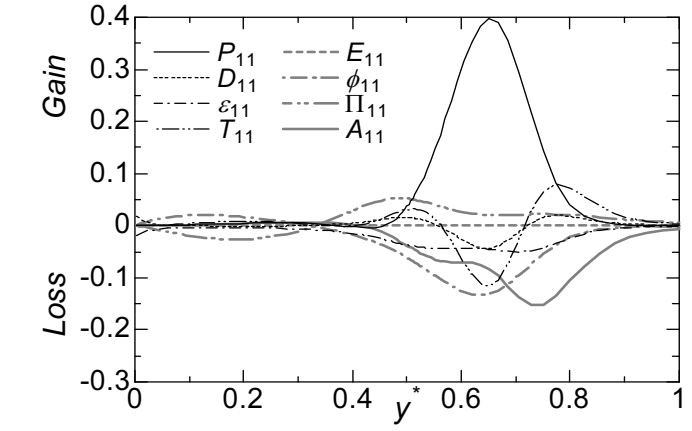

a

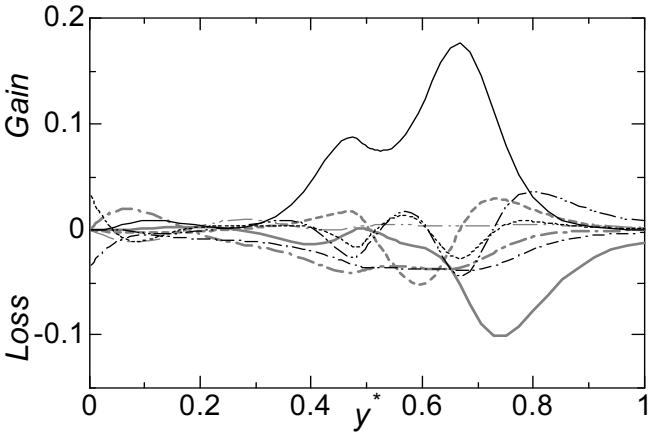

b

Figure 12: Budget of Reynolds stress $\overline{u'^+u'^+}$ at $x^* = 7.5$. (a) Newtonian-fluid flow, (b) Viscoelastic-fluid flow ($We_{\tau 0} = 20$).

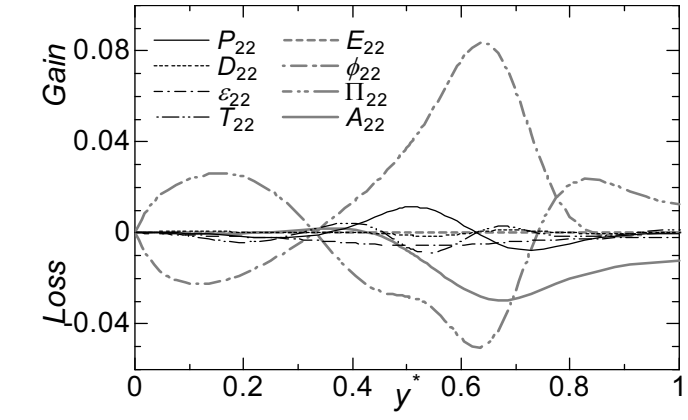

a

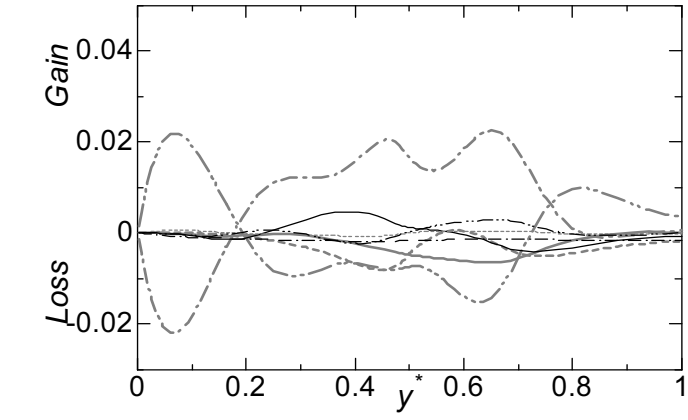

b

Figure 13: Same as Fig. 12, but for $\overline{v'^+v'^+}$.

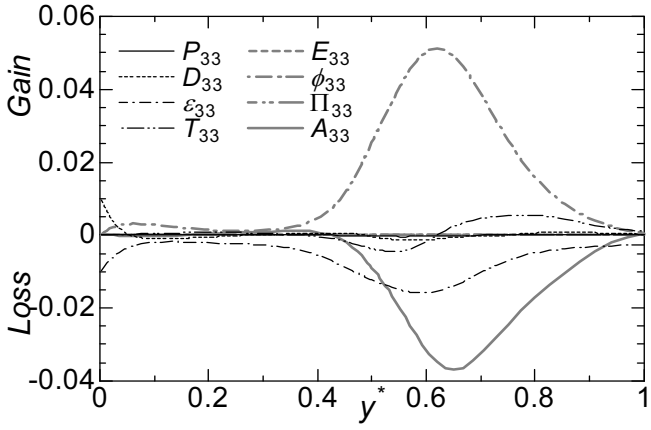

a

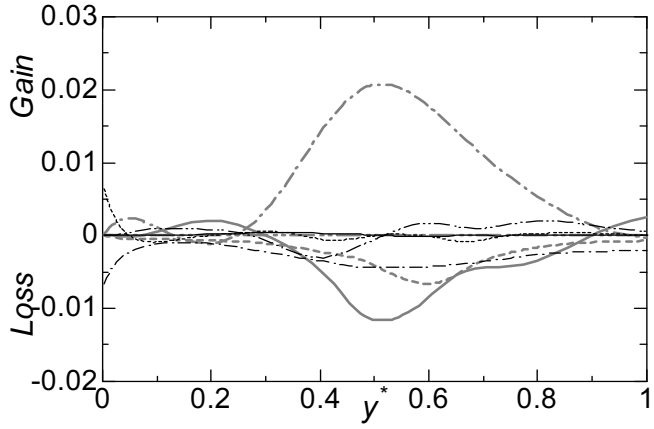

b

Figure 14: Same as Fig. 12, but for $\overline{w'^+ w'^+}$.

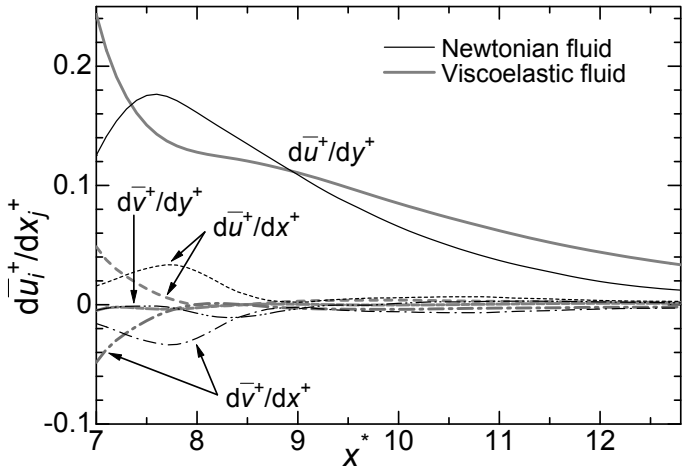

Figure 15: Streamwise distributions of velocity gradient at $y^* = 0.5$.

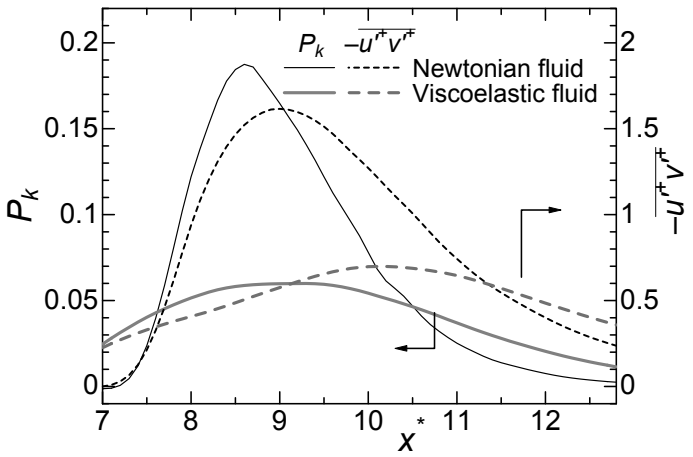

Figure 16: Streamwise distributions of turbulent kinetic energy production, P_k, and Reynolds shear stress, $\overline{u'^+v'^+}$ at $y^* = 0.5$.